A Novel Phase Unwrapping Method for Low Coherence Interferograms in Coal Mining Areas Based on a Fully Convolutional Neural Network

Yu Yang, Bingqian Chen, Zhenhong Li, *Senior Member, IEEE*, Chen Yu, Chuang Song, and Fengcheng Guo

***Abstract*—Subsidence caused by underground coal mining activities seriously threatens the safety of surface buildings, and interferometric synthetic aperture radar has proven to be one effective tool for subsidence monitoring in mining areas. However, the environmental characteristics of mining areas and the deformation behavior of mining subsidence lead to low coherence of interferogram. In this case, traditional phase unwrapping methods have problems, such as low accuracy, and often fail to obtain correct deformation information. Therefore, a novel phase unwrapping method is proposed using a channel-attention-based fully convolutional neural network (FCNet-CA) for low coherence mining areas, which integrates multiscale feature extraction block, bottleneck block, and can better extract interferometric phase features from the noise. In addition, based on the mining subsidence prediction model and transfer learning method, a new sample generation strategy is proposed, making the training dataset feature information more diverse and closer to the actual scene. Simulation experiment results demonstrate that FCNet-CA can restore the deformation pattern and magnitude in scenarios with high noise and fringe density (even if the phase gradient exceeds π). FCNet-CA was also applied to the Shilawusu coal mining area in Inner Mongolia Autonomous Region, China. The experimental results show that, compared with the root mean square error (RMSE) of phase unwrapping network and minimum cost flow, the RMSE of FCNet-CA in the strike direction is reduced by 67.9% and 29.5%, respectively, and by 72.4% and 50.9% in the dip direction, respectively. The actual experimental results further verify the feasibility and effectiveness of FCNet-CA.**

***Index Terms*—Decorrelation, deep learning, interferometric synthetic aperture radar (InSAR), mining subsidence, phase unwrapping.**

I. Introduction

COAL, as the primary energy source worldwide, holds immense strategic value for the growth of the global economy. Still, extensive underground coal mining can lead to severe land subsidence and potential environmental disasters [1]. For example, between 1949 and 2002, coal mining in China resulted in land subsidence exceeding 700 000 ha in total area, and the resulting economic loss exceeded 7 billion USD [2]. Monitoring surface subsidence regularly in mining regions enables an understanding of surface deformation patterns and provides a basis for decision-making in preventing and controlling surface subsidence disasters. Traditional monitoring techniques include leveling, global positioning system monitoring, and other methods. Although their monitoring accuracy is high, these methods have limitations, such as high cost, substantial labor requirements, and point measurements only.

The emergence of interferometric synthetic aperture radar (InSAR) provides one novel tool to monitor surface subsidence in mining areas. This technology has outstanding advantages, such as rapid speed and high precision, and it has achieved many successful cases in monitoring of mining subsidence [3], [4], [5]. Phase unwrapping is one crucial procedure in InSAR processing, and its results determine the reliability and accuracy of subsequent deformation. Traditional phase unwrapping methods [6], [7], [8] assume that the absolute phase difference (phase gradient) value between two adjacent points to be unwrapped should be less than π [9]. However, the surface of the mining area is mainly covered by sparse vegetation and bare soil, the

Manuscript received 3 August 2023; revised 4 October 2023; accepted 9 November 2023. Date of publication 15 November 2023; date of current version 29 November 2023. This work was supported in part by the Natural Science Foundation of China under Grant 42374020 and Grant 62101219, in part by the China Postdoctoral Science Foundation under Grant 2019M663601, in part by the Shaanxi Province Science and Technology Innovation team under Grant 2021TD-51, in part by the Fundamental Research Funds for the Central Universities, CHD under Grant 300102263510, in part by the European Space Agency through the ESA-MOST DRAGON-5 project under Grant 59339, in part by the International Cooperation and Exchanges National Natural Science Foundation of China under Grant 41920104010, and in part by the Postgraduate Research & Practice Innovation Program of Jiangsu Normal University under Grant 2022XKT0124. *(Corresponding authors: Bingqian Chen; Zhenhong Li.)*

Yu Yang and Fengcheng Guo are with the School of Geography, Geomatics and Planning, Jiangsu Normal University, Xuzhou 221116, China (e-mail: 2020211465@jsnu.edu.cn; fchguo@jsnu.edu.cn).

Bingqian Chen is with the School of Geography, Geomatics and Planning, Jiangsu Normal University, Xuzhou 221116, China, also with the College of Geological Engineering and Geomatics, Chang'an University, Xi'an 710054, China, and also with the Key Laboratory of Western China's Mineral Resource and Geological Engineering, Ministry of Education, Xi'an 710054, China (e-mail: bqccumt@gmail.com).

Zhenhong Li is with the College of Geological Engineering and Geomatics, Chang'an University, Xi'an 710054, China, also with the Key Laboratory of Western China's Mineral Resource and Geological Engineering, Ministry of Education, Xi'an 710054, China, also with the Big Data Center for Geosciences and Satellites, Xi'an 710054, China, and also with the School of Engineering, Newcastle University, NE1 7RU Newcastle Upon Tyne, U.K. (e-mail: zhenhong.li@chd.edu.cn).

Chen Yu and Chuang Song are with the College of Geological Engineering and Geomatics, Chang'an University, Xi'an 710054, China, and with the Key Laboratory of Western China's Mineral Resource and Geological Engineering, Ministry of Education, Xi'an 710054, China, and also with the Big Data Center for Geosciences and Satellites, Xi'an 710054, China (e-mail: chen.yu@chd.edu.cn; chuang.song@chd.edu.cn).

Digital Object Identifier 10.1109/JSTARS.2023.3333277

coherence is low, and the interferometric phase is often discontinuous. At the same time, in the coal mining process, there is large surface displacement in a very small range, resulting in dense interferometric fringes, and the deformation gradient often exceeds π. The above reasons make it difficult for the phase continuity assumption to be satisfied in mining areas.

Deep learning is a hot research topic in machine learning, which can analyze and predict by learning the inherent laws of sample data [10]. It has been successfully applied in the field of InSAR, such as phase denoising [11], [12], [13], target detection [14], [15], [16], and other applications [17], [18], [19]. Concomitantly, deep-learning methods have also achieved mass applications in InSAR single-baseline phase unwrapping (SBPU) [20], [21] and multibaseline phase unwrapping [22], [23], [24]. According to the number of unwrapping steps, the deep-learning-based SBPU can be classified as either one-step or two-step [25]. The one-step phase unwrapping method uses the deep-learning network to restore the wrapped phase to the absolute phase directly; that is, the input is the wrapped phase and the output is the absolute phase, and no other processing steps are required. A one-step deep-learning phase unwrapping (DLPU) method was proposed by Wang et al. [26]. However, the presence of noise in the SAR interferogram may seriously affect the performance of DLPU. Inspired by the classical denoising convolutional neural network, Wu et al. [27] proposed the phase unwrapping network (PUNet). However, this method can lead to large phase unwrapping errors if interferograms are affected by severe temporal decorrelation. Based on the conditional generative adversarial network, Zhou et al. [28] proposed a novel phase unwrapping method (referred to as PU-GAN). It can guarantee the congruency between the rewrapped interferometric fringes of the unwrapped phase and the original interferogram, which is the apparent advantage of PU-GAN. However, the training dataset of the PU-GAN network mainly covers the terrain phase in the interferogram, which leads to its relatively weak generalization ability and may not be able to unwrap the interferogram of the mining area. The two-step phase unwrapping method usually calculates integer ambiguity of the interferogram phase at any pixel or absolute phase gradient between adjacent pixels and then retrieves the absolute phase through mathematical operations, e.g., least squares (LS). The PhaseNet [29], [30] is representative of two-step phase unwrapping. This method regards phase unwrapping as a semantic segmentation problem; that is, it first predicts the phase ambiguity number of each pixel and then adds it to each pixel to obtain the absolute phase. However, PhaseNet is mainly suitable for clean and noise-free interferograms and does not work well for SAR interferograms with long temporal baselines and low coherence. Zhou et al. [31] proposed the phase gradient net phase unwrapping method to accurately estimate the interferometric phase gradient and employ the LS algorithm to retrieve the absolute phase. This method can accurately obtain the phase gradient under different noise levels and terrain features. Still, for the interferogram of the subsidence area of the mining area, this method cannot predict the phase gradient well, which leads to further propagation of errors in the subsequent phase integration process.

The surface of the mining area is often covered by sparse vegetation, resulting in temporal decorrelation and severe noise. In addition, one typical characteristic of mining activity is that a large ground surface displacement in a small range results in a large deformation gradient that tends to exceed π. Severe noise and large deformation gradient lead to low coherence of interferogram in the mining area, which often fails the traditional phase unwrapping method. Therefore, a fully convolutional neural network with channel attention (FCNet-CA) is proposed in this article to unwrap interferograms with low coherence in mining areas. This method combines channel attention and multiscale feature extraction modules to extract interferometric phase features better. Residual connections and bottlenecks are added inside the module to train a deeper network while saving training time. In addition, based on the mining subsidence prediction model and transfer learning method, a new sample generation strategy in the mining subsidence scene is proposed, making the training dataset feature information more diverse and closer to the actual scene. Datasets with different noise and deformation gradients are simulated to test the feasibility of FCNet-CA. FCNet-CA is then applied to the Shilawusu mining area in Inner Mongolia Autonomous Region, China, and the results further verify the precision and reliability of the proposed method.

II. Methodology

A. Generation of the Training Datasets

The quality of training samples largely determines the reliability of network predictions. Therefore, generating simulated training samples close to the actual scene significantly improves the network performance. Existing methods often only use a specific function to simulate the surface subsidence of mining areas, such as the two-dimensional (2-D) Gaussian surface method proposed by Wu et al. [27]. However, this function model is only an approximate expression of the surface subsidence in the mining area without considering the influence of the mining area's geological and mining conditions, resulting in a weak generalization ability of the model. Therefore, this article proposes a new sample generation method for mining subsidence. Two datasets were generated in the experiment, on the one hand, a specific function (i.e., a 2-D Gaussian surface function) is used to simulate deformation, which is called dataset *G*. It combines complex Gaussian noise, Perlin noise, and water decorrelation noise to generate samples. In addition, combined with the mine geology and mining conditions, the mining subsidence prediction model is used to simulate deformation and integrate the same noise to create supplementary samples called dataset *M*. 2-D Gaussian surface function is expressed as

$$p\left(X|u,\Sigma\right)=\frac{1}{2\pi|\Sigma|^{\frac{1}{2}}}\exp\left(-\frac{\left(X-u\right)^{T}\Sigma^{-1}\left(X-u\right)}{2}\right) \quad (1)$$

where $X=[x_1,x_2]^T$ represents 2-D grid and $u=[u_1,u_2]^T$ represents the location of the deformation area. Σ is a 2-D covariance matrix that controls the size and shape of the deformation area.

However, in the actual mining scene, the deformation of the mining area is not a standard oval shape. Therefore, it is necessary to randomly distort the 2-D Gaussian surface to better simulate the interferometric phase of the mining area

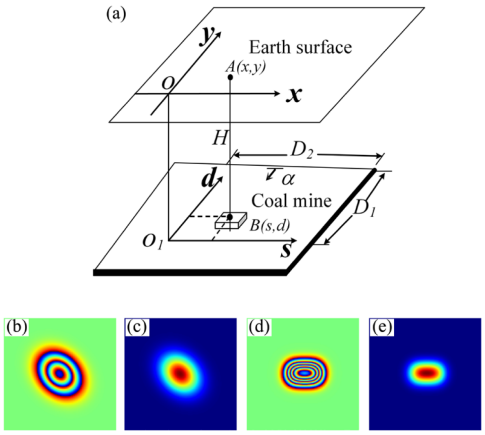

Fig. 1. (a) Local coordinate systems for coal mining, modified from [2], (b) example of surface deformation generated by the two-dimensional Gaussian surface method, (c) wrapped phase of (b), (c) example of surface deformation generated by the mining subsidence prediction model, and (d) wrapped phase of (c).

in the sample simulation process. Assume that on the $N \times N$ interferogram, there are $n \times n$ random control points, which control the direction and magnitude of surface distortion through a random matrix. The distortion formula is expressed as

$$\phi_x = \lambda \cdot \sum \left(V_x^{n\times n} * I\right) \tag{2}$$

$$\phi_y = \lambda \cdot \sum \left(V_y^{n\times n} * I\right) \tag{3}$$

where λ is the degree of distortion; ($V_x^{n\times n}$, $V_y^{n\times n}$) is a random matrix; and I represents the magnitude of every control point.

Fig. 1(a) shows the principle of training samples generated with the mining subsidence prediction model. According to mining subsidence theory [32], the total subsidence $W_a(x, y)$ of point $A(x, y)$ caused by exploiting the whole working panel is expressed as

$$W_a(x,y) = W_0 \int_{s_3}^{l} \int_{s_1\cos\alpha}^{L} \frac{1}{r^2} e^{-\pi \frac{(x-s)^2+(y-d)^2}{r^2}} \mathrm{d}v\mathrm{d}u \tag{4}$$

where $W_0 = mq\cos\alpha$, m is the thickness of the coal seam, q represents the subsidence factor, and α is the inclination of the coal seam. $l = D_2 - s_4$ and $L = (D_1 - s_2)\cos\alpha$. D_1 and D_2 represent the length and width of the working panel, respectively. For a specific mining area, the above parameters are all fixed values. r, s_1, s_2, s_3, and s_4 are the known parameters of the subsidence model in the simulation process. s and d are the corresponding coordinates of mining unit element B. Fig. 1(c) and (e) shows the examples of two different deformation samples generated by the 2-D Gaussian surface and mining subsidence prediction model, and Fig. 1(b) and (d) is the wrapped phase of Fig. 1(c) and (e).

The main parameters used in the sample simulation process are shown in Table I and a total of 30 000 training samples (sample size is 128×128) were generated through the proposed methods, of which 80% were generated with 2-D Gaussian surface function [26], and the remaining 20% were generated with the mining subsidence model.

TABLE I
MAIN PARAMETERS OF THE SIMULATED SAMPLES

Parameters	Range
q	(0.3, 1)
H/r	(1.5, 3)
s_1=s_2=s_3=s_4 (m)	(0, 60)
m (m)	(1.5, 10.5)
α (degree)	(2, 20)
λ	5
I	20

B. Construction of the Neural Network

FCNet-CA is one fully convolutional neural network (as shown in Fig. 2), and it can theoretically accept the input of any image size [33]. FCNet-CA uses batch normalization layers to avoid the issues of gradient vanishing and overfitting that may arise due to excessive network depth [34]. Existing phase unwrapping methods based on deep-learning networks often do not fully use multilevel feature information, which affects the accuracy of phase unwrapping results. Therefore, the multiscale feature fusion (MFF) block is built into the network to fuse convolutional kernels with varying dilation rates to extract interferometric phase features better. In general, as the dilation rate increases, so does the extent of the receptive field, while the network parameters will not increase [35]. However, with an increase in the dilation rate, the convolution kernel becomes sparser, and the phase feature extraction ability will also be affected. In the experiment, 1, 2, and 3 are selected as the thresholds for the fusion of convolutional layers with different dilation rates, respectively. Squeeze-and-excitation (SE) block [36] is used in the network to select essential features better and pay attention to the differences between different levels of features. The SE block (as shown in Fig. 3) allows the network to autonomously perform phase feature recalibration, using the global information of the interferogram to emphasize key phase features and suppress useless features selectively. A bottleneck block (the black dashed box in Fig. 2) is included in the network to decrease the network's parameters and help to build a deeper network [37]. In addition, by utilizing residual connection (the blue line in Fig. 2), shallow and in-depth information is added to avoid the loss of phase characteristics caused by the network in the transmission process [38].

As shown in Fig. 2, the first layer of FCNet-CA extracts 64 feature maps from the input interferogram layer using a 2-D convolution layer. Ten MFF and squeeze-and-excitation (MFSE) blocks are used for phase feature extraction. Each MFSE block consists of an MFF block and an SE block. Then, the absolute phase information is reconstructed by ten bottleneck blocks, and finally, the absolute phase is output by two convolution layers. In convolutional neural networks, the convolutional layer is often one of the layers with the largest amount of computation. Although a large convolution kernel will bring about an increase in the receptive field, it is often accompanied by an increase in the amount of computation, resulting in low training

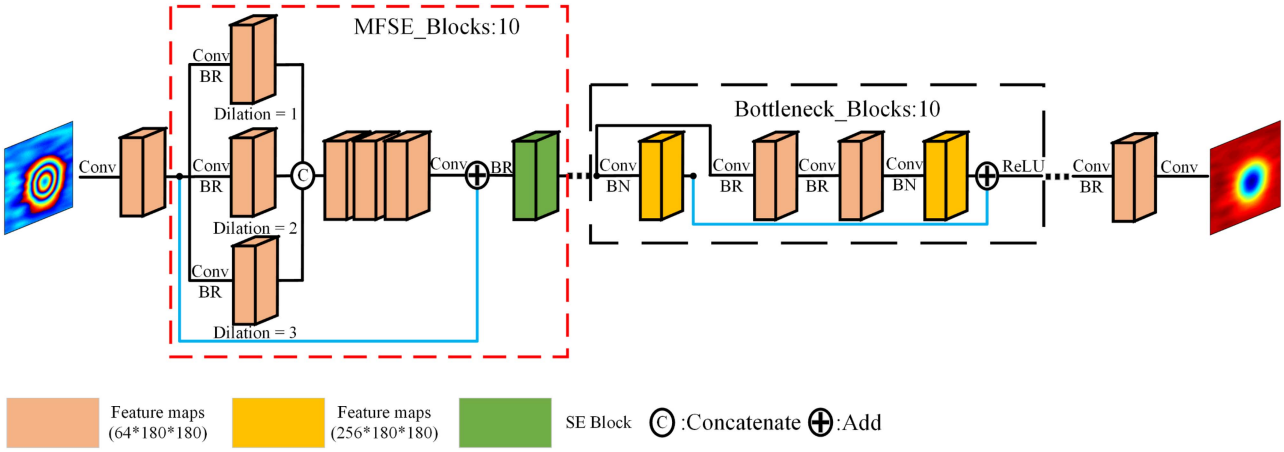

Fig. 2. Proposed networks' structure. Conv represents the convolution layer, and BR is the operation of batch normalization and rectified linear unit (ReLU), respectively. The blue line represents the operation of the residual connection.

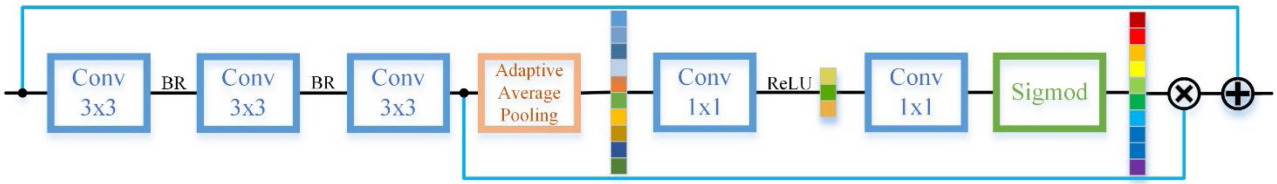

Fig. 3. Overview of the SE block.

efficiency. The receptive field of the large convolution kernel is equivalent to the receptive field superimposed by multiple small convolution kernels. For example, the receptive field of a 5×5 convolution kernel is equal to the receptive field obtained by the superposition of two 3×3 convolution kernels. In addition, the 3×3 convolution kernel is the smallest size that can capture the pixel features of the surrounding eight fields and has a better effect in capturing the local features of the input image [39]. Therefore, to improve the training efficiency and better phase feature extraction ability, each convolution kernel in the network is uniformly set to 3×3.

C. Training of the Neural Network

One of the keys to recovering absolute phases directly from low coherence interferograms through convolutional neural networks is the quality of the training dataset. Considering the absolute phase corresponding to the deformation of the mining area cannot be directly obtained, the simulated datasets are used to train FCNet-CA in the experiment. The training process consists of four parts: sample set production, network training, transfer learning, and output of prediction results. The specific steps are described as follows.

Step 1. Production of sample datasets: As mentioned above, two datasets were produced in the experiment. One dataset uses a 2-D Gaussian surface function, complex Gaussian noise, Perlin noise, and water decorrelation noise to simulate the interferogram called dataset *G*. The other uses the proposed method, that is, uses the mining subsidence model to simulate deformation and then combines the same noise to simulate the interferogram called dataset *M*.

Step 2. Network training: First, the weight of FCNet-CA is initialized. Weight initialization can help accelerate the network's convergence and avoid the gradient's disappearance or explosion in the network feedforward process. The dataset *G* is then segmented, 80% for training and 20% for testing. Finally, the training dataset is iteratively trained to ensure the convergence trend of loss value, and the network weight with the highest evaluation accuracy on the validation dataset is retained.

Step 3. Transfer learning: Transfer learning is a machine-learning method in which a pretrained model is reused for another task [40]. Through transfer learning, the learned model parameters (knowledge learned by the model) can be shared with the new model in some way to speed up and optimize the learning efficiency of the model. Here, transfer learning enables FCNet-CA to use the rules of phase feature extraction learned on dataset *G* to reconstruct the absolute phase information of dataset *M*. This way, FCNet-CA can be easily applied to new phase unwrapping scenarios, saving much retraining time. Specifically, FCNet-CA is retrained on dataset *M* after loading the pretraining weight obtained on dataset *G*. Freezing the parameters of the phase feature extraction part and only updating the parameters of the phase reconstruction part to gain the final trained network.

Step 4. Output of prediction results: Based on the final trained network in step 3, FCNet-CA can directly predict the absolute phase of the actual deformation in the mining area. The flowchart of the complete training process is shown in Fig. 4.

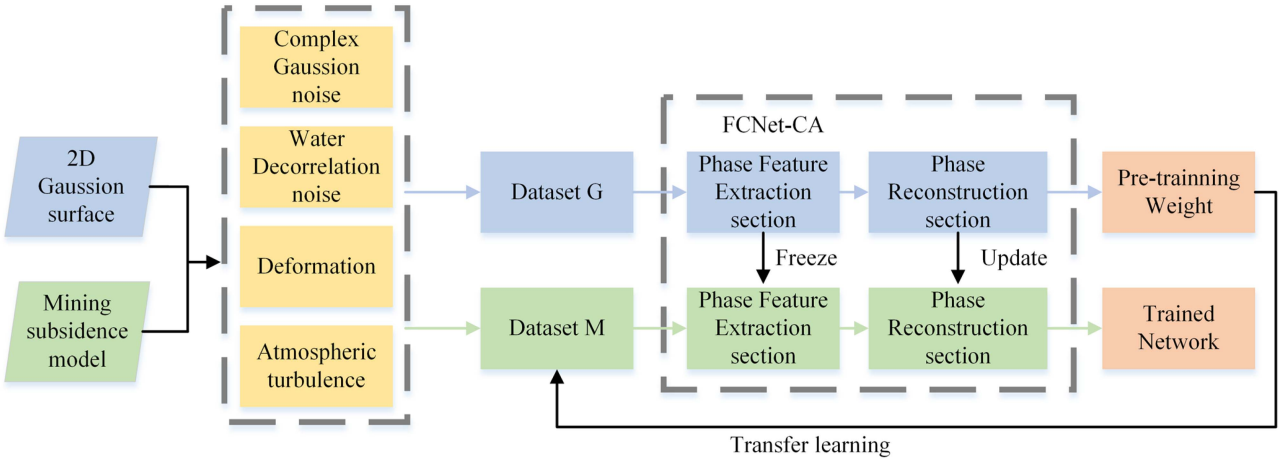

Fig. 4. Training process of the FCNet-CA.

D. Selection of the Loss Function

The loss function is used to measure how far the model's predicted value deviates from the actual value. In the experiment, the Huber function [41] is selected as the loss function for the training set and validation set, and its corresponding formula is expressed as

$$L(\theta) = \begin{cases} \frac{1}{2}(\hat{\varphi}_i - Y(\varphi_i;\theta))^2, & |\hat{\varphi}_i - Y(\varphi_i;\theta)| < \gamma \\ \gamma(|\hat{\varphi}_i - Y(\varphi_i;\theta)| - \frac{1}{2}\gamma), & \text{otherwise} \end{cases} \quad (5)$$

where θ is a trainable parameter in the network. $Y(\varphi_i; \theta)$ is the result of each round of network prediction of the ith pixel and $\hat{\varphi}_i$ is the corresponding reference result. γ is a given hyperparameter set to 1 in the experiment. It can be seen from Formula (5) that when $|\hat{\varphi}_i - Y(\varphi_i;\theta)| < \gamma$, Formula (5) becomes close to the mean square error (MSE). When $|\hat{\varphi}_i - Y(\varphi_i;\theta)| > \gamma$, Formula (5) is similar to the mean absolute error (MAE). Therefore, the Huber loss function combines the benefits of both MSE and MAE while reducing sensitivity to outliers.

III. Experiments

A. Simulation Experiment

The training equipment parameters are as follows: FCNet-CA is developed with Python 3.9 and PyTorch 1.11.0. The device contains an Intel(R) i7-12700F (CPU), 32 GB RAM, and NVIDIA GeForce RTX 3090 (GPU). The adaptive moment estimation with a weight decay optimizer is used in network training. The learning rate is set at 0.0001, the number of training epochs is selected at 120, the minibatch size is 16, and the training time is approximately 60 h.

The trained FCNet-CA is applied to the independently generated simulation dataset. The test dataset contains 3000 simulated interferograms equally distributed between the subsidence and the 2-D Gaussian surface model's samples. The deformation magnitude from -15π to 15π, the complex Gaussian noise from 0 to 2π, and the water decorrelation noise from π to 3π are randomly added to each simulated interferogram, respectively. The standard deviation (STD) and maximum error in phase ambiguity number ε (represents the maximum error between the predicted phase and the reference phase divided by 2π) are utilized as assessment indexes. To compare the performance of the proposed method with the existing algorithms, branch cut (BC) [6], quality-guided PU (QGPU) [7], minimum cost flow (MCF) [8], phase unwrapping max-flow algorithm (PUMA) [42], LS [43], DLPU [26], PUNet [27], and proposed method in this article are used for the unwrapping experiment. To test the antinoise performance of the different methods, every method is used to unwrap the test dataset which contains noise. The results obtained by other methods are sorted with the MCF results as a reference, and Fig. 5(a) shows the results of the STD comparison of eight methods. From Fig. 5(a), it can be seen that the STD of FCNet-CA is significantly smaller compared to the traditional

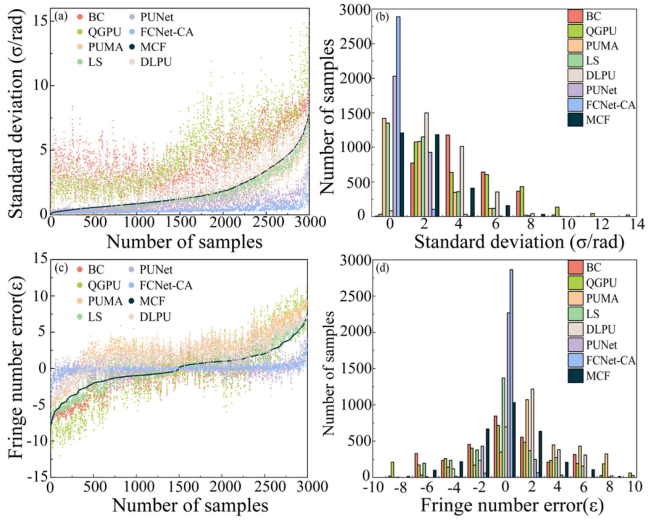

Fig. 5. Error statistics of different unwrapping methods on 3000 simulated interferograms. (a) STD distribution of different unwrapping methods. (b) STD distribution statistics of different unwrapping methods. (c) Fringe number error distribution of different unwrapping methods. (d) Fringe number error distribution statistics of different unwrapping methods. Note that for better visualization, a mean filter of size five is applied to the results in Fig. 5(a) and (c), and the navy blue curves represent the MCF unwrapping results.

TABLE II
RUNTIME OF DIFFERENT ALGORITHMS

Algorithms	Time(s)
BC	540
QGPU	1320
LS	1020
PUMA	690
MCF	300
DLPU	60
PUNet	620
FCNet-CA	210

methods (BC, QGPU, MCF, PUMA, and LS). Fig. 5(b) shows that FCNet-CA has the highest percentage of STD less than π, with a value of 99.5%, and the average STD of FCNet-CA is 0.4 rad, which is 68.8%, 87.3%, 79.7%, 86.6%, 80.5%, 90.6%, and 93.8% lower than that of PUNet, DLPU, MCF, LS, PUMA, BC, and QGPU, respectively.

Fig. 5(c) shows that in comparing the maximum unwrapping errors (MUEs) in fringe numbers, the result obtained by FCNet-CA is much smaller than that of the other seven methods. The average absolute MUEs in fringe numbers is 0.44, received by FCNet-CA, which has the best performance, followed by PUNet with 1.79, MCF with 2.13, DLPU with 2.71, LS with 2.89, PUMA with 3.75, BC with 3.86, and QGPU with 6.25. In addition, the percentage of samples with $|\varepsilon| \leq 1$ for FCNet-CA reaches 91.3%, which is significantly higher than the 53% of PUNet, 28.3% of MCF, 24.3% of DLPU, 13.3% of LS, 7.8% of PUMA, 6.3% of BC, and 1.9% of QGPU, further illustrating the reliability of FCNet-CA. However, Fig. 5(d) shows that each method has misestimated the absolute phase to different degrees. If the unwrapping samples with $|\varepsilon| > 2$ are regarded as the result of severe misestimation of the absolute phase, the misestimation percentages of MCF, BC, QGPU, PUMA, LS, DLPU, PUNet, and FCNet-CA are 37.6%, 77.8%, 93.8%, 72.9%, 59.2%, 49.6%, 33.4%, and 2.2%, which indicate the strong robustness of FCNet-CA.

In summary, the traditional methods (BC, QGPU, LS, MCF, and PUMA) cannot perform correct unwrapping with increased noise and will seriously misestimate the absolute phase. The performance of MCF is marginally superior to that of the other traditional phase unwrapping methods. Furthermore, the deep-learning method, i.e., DLPU, cannot learn the relationship between the wrapped phase and the absolute phase well due to the noise. Another deep-learning method, i.e., PUNet, can overcome the shortcomings of traditional methods to a certain extent, but the misestimation phenomenon still exists. Compared with PUNet, the misestimation rate of FCNet-CA is further reduced, the unwrapping accuracy is improved by 68.8%, and 91.3% of the fringe error is limited to approximately 0. In addition, the running time of different algorithms on all testing data shows (Table II) that the FCNet-CA method has higher computational efficiency and can achieve a better balance between accuracy and efficiency.

To visually display the performance of FCNet-CA, BC, QGPU, PUMA, LS, MCF, DLPU, PUNet, and FCNet-CA are used to unwrap six samples with different deformation gradients and noise levels. Fig. 6(a) shows unwrapping results and corresponding unwrapping errors obtained by eight methods in the samples with varying noise levels. It can be seen from Fig. 6(a) that every method can recover the deformation pattern and deformation magnitude entirely in the case where the noise level is relatively low [sample 1 of Fig. 6(a)]. But when the noise level increases [sample 2 of Fig. 6(a)], BC, QGPU, and LS can only recover the deformation value of some edge regions but not the deformation pattern and deformation magnitude of the deformation center. The recovery abilities of PUMA and MCF are the best in the traditional methods, and they can recover the deformation pattern and magnitude of the deformation center. Compared with traditional methods, DLPU, PUNet, and FCNet-CA also have great recovery results on the deformation center. Still, visually it seems that the unwrapping phase of FCNet-CA is closer to the absolute phase. The interferogram's center fringe is blurred when the noise level is further increased [sample 3 of Fig. 6(a)]. In this case, all traditional unwrapping methods except MCF cannot recover the absolute phase of the deformation center, which implies that MCF has the best antinoise ability in traditional methods. Estimating the deformation center by DLPU and PUNet also shows some errors. In contrast, the recovery results of FCNet-CA on the deformation center and edge are still better than those of other methods, whose results are closest to the absolute phase.

When the noise level exceeds 0.8π, the noise level in sample 2, most traditional methods fail to unwrap the simulated interferogram, suggesting that 0.8π is the maximum acceptable noise level for most methods (BC, QGPU, LS, and PUMA). Under the noise level of 0.8π, the robustness of different methods to the deformation gradient is tested by increasing the maximum deformation gradient, as shown in Fig. 6(b). By observing Fig. 6(b), it can be found that the coherence in the deformation area becomes lower as the maximum deformation gradient increases, and all the traditional methods fail to recover the deformation pattern and deformation magnitude of the deformation center. The noise level and maximum deformation gradient of sample 4 are close to sample 2, so they have similar unwrapping results. The interferogram's center fringe is blurred and not continuous in sample 5 and sample 6, only the deep-learning-based method can unwrap successfully. Compared with two other deep-learning-based methods, the unwrapping results obtained by FCNet-CA are most similar to the absolute phase.

The root mean square error (RMSE) values of each unwrapping method are calculated to assess the performance of the eight methods (Table III). It can be seen from Table III that even if the noise is low and the fringes are clear (sample 1), the RMSE of FCNet-CA is smaller than the other methods. As the noise in sample 2 and sample 3 becomes more severe, the RMSEs of traditional methods, such as BC, QGPU, LS, and PUMA, increase significantly. In contrast, those of MCF and the deep-learning methods (DLPU, PUNet, and FCNet-CA) remain relatively low. The maximum deformation gradient gradually increases in samples 4–6, where the maximum deformation gradient of sample 6 exceeds π rad/pixel. Due to the relatively large deformation gradient, the coherence of the deformation center is low (sample

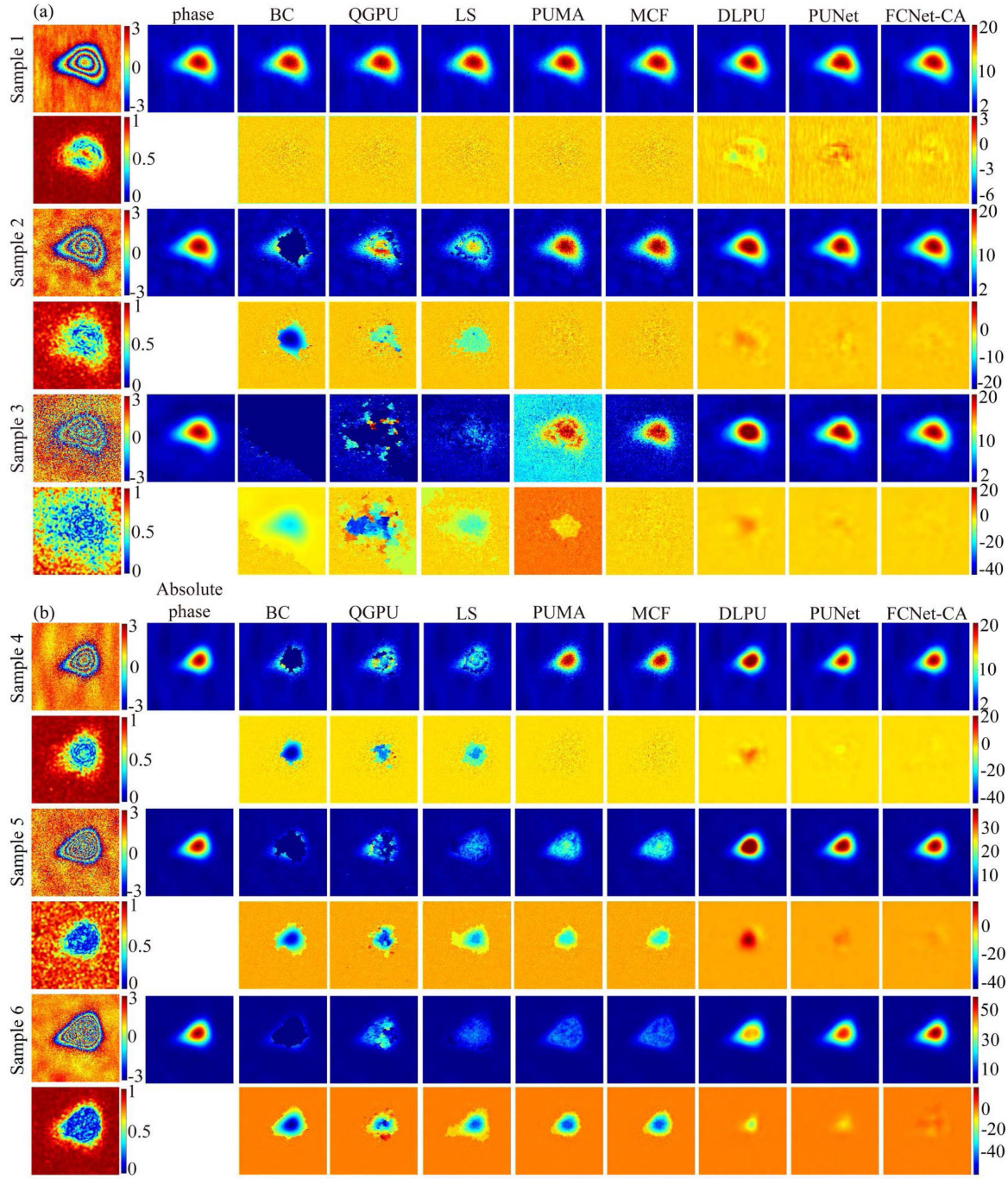

Fig. 6. Performance of different methods with different noise levels and fringe density. (a) Maximum deformation gradient of samples 1–3 is all 1 rad/pixel, but the noise levels are different, which are 0.3π, 0.8π, and 1.3π, respectively. (b) Noise levels of samples 4–6 are all 0.8π but the maximum deformation gradients are different, which are 1.1, 2.1, and 3.3 rad/pixel, respectively. The upper row of each sample is the unwrapping results of each method, and the lower row is the corresponding unwrapping errors.

4), and there are even decorrelation areas in the center (samples 5–6). All methods except for the deep-learning-based method can no longer retrieve the unwrapped phase correctly. Compared with other methods, FCNet-CA always shows excellent unwrapping performance, and the RMSE is lower than that of DLPU and PUNet, indicating that FCNet-CA is more effective and robust to severe noise and large deformation gradient.

In practical scenarios of mining subsidence, the deformation center often includes dense fringes and serious decorrelation noise, which is the main reason for the failure of existing unwrapping methods. The above analysis shows that FCNet-CA can be applied to clean or noisy interferograms, accurately recover the absolute phase, and ensure that unwrapping errors remain relatively low.

To test the sensitivity of FCNet-CA to the deformation gradient, the mining subsidence model is used to simulate the deformation sample set, and the maximum deformation gradient is equally distributed from 0 to 4.8 rad/pixel. The model parameters

TABLE III
RMSES OF DIFFERENT METHODS

Methods / samples	BC	QGPU	LS	PUMA	MCF	DLPU	PUNet	FCNet-CA
Sample 1	0.4042	0.4045	0.2877	0.2772	0.2777	0.2539	0.1994	**0.1421**
Sample 2	4.1046	1.8936	1.9978	0.6960	0.6904	0.3085	0.1850	**0.1347**
Sample 3	4.7536	9.9229	4.0137	6.2004	1.2902	0.7271	0.2783	**0.2109**
Sample 4	3.2198	2.0656	1.9685	0.5559	0.5484	0.4431	0.1455	**0.0933**
Sample 5	6.3576	5.2980	4.1416	3.0047	2.9434	1.9476	0.3706	**0.2071**
Sample 6	9.7348	6.2712	6.7155	6.5677	6.5399	1.5974	0.8574	**0.3987**

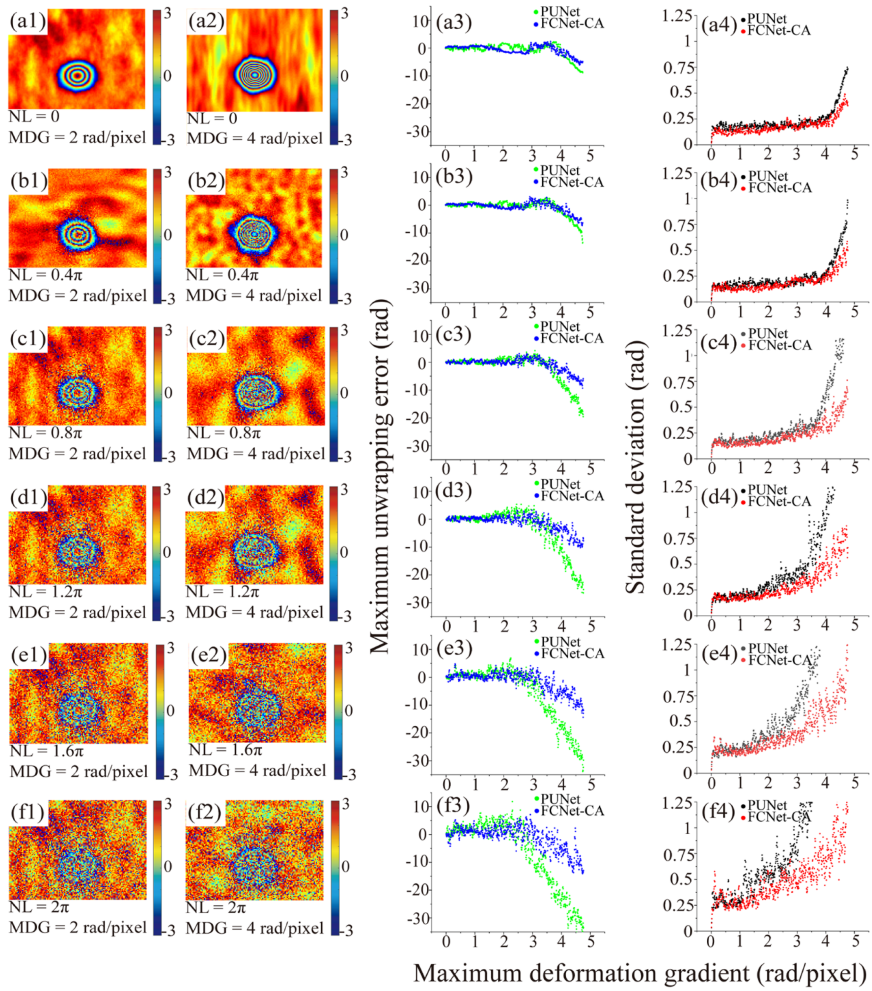

Fig. 7. Maximum unwrapping errors and STD results of FCNet-CA and PUNet on the 3750 interferograms with different maximum deformation gradients and noise levels. The first two columns of (a)–(f) present synthetic interferograms with a deformation gradient of 2 and 4 rad/pixel under different noise levels, respectively. The last two columns of (a)–(f) are the distribution of maximum unwrapping errors and STD results of FCNet-CA and PUNet, respectively. NL represents noise level and MDG represents maximum deformation gradient.

are selected as follows: sink factor q is set to 0.6, H/r is 2, the offsets of the inflection points $s_1 = s_2 = s_3 = s_4$ is 16 m, and the inclination of the coal seam is 5°, the thickness of the coal seam is 3 m, and the length and width of the working panel are 80 and 10 m. The above parameters fix the shape and size of the subsidence region. The complex Gaussian noise from 0 to 2π is added to the interferograms of different deformation gradients to explore the maximum deformation gradient that FCNet-CA can recover under different noise levels. Finally, a total of 3750 simulated interferograms were generated.

The evaluation results with different maximum deformation gradients and noise levels are shown in Fig. 7(a)–(f). The first two columns are the display of simulated interferograms with different deformation gradients under different noise levels, and the last two columns are the MUEs and STD of FCNet-CA and PUNet. It can be seen from Fig. 7 that as the noise level increases (from top to bottom), MUE and STD become more divergent, and the maximum deformation gradient that can be recovered is smaller, which implies that the maximum deformation gradient that the two methods can recover depends on the noise level.

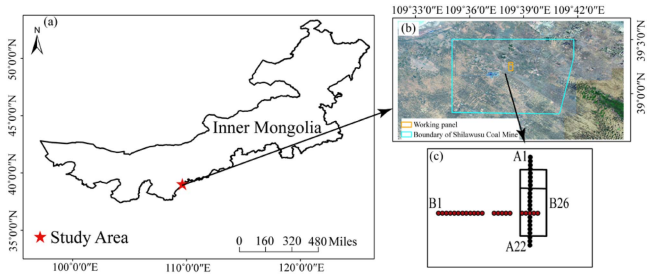

Fig. 8. Overview of the study area. (a) Is the location of the study area, (b) is the working panel's position, and (c) is the layout of the observation station. Red points represent the leveling observation stations along the dip direction, and black points represent the leveling observation stations along the strike direction. Note that leveling data were collected using an OPTONS3 electronic level with an accuracy of ± 3 mm for every kilometer round trip.

In terms of STD tolerance of 0.25 rad, for interferograms with the noise level equal to 0, the maximum deformation gradient recovered by these two methods exceeds π rad/pixel and reaches 4.1 rad/pixel. Traditional methods often have poor unwrapping results or fail to unwrap under this deformation gradient. When the noise level comes to 0.4π, the maximum recoverable deformation gradient of FCNet-CA still exceeds π rad/pixel and reaches 3.7 rad/pixel, while the maximum recoverable deformation gradient of PUNet is close to π rad/pixel. As the noise level comes to 0.8π, as shown in Fig. 7(c1)–(c4), although the recoverable deformation gradient of FCNet-CA becomes smaller, i.e., π rad/pixel, the results are still more satisfied than PUNet and the traditional unwrapping methods, as conventional methods assume that the absolute phase difference (phase gradient) value between two adjacent points to be unwrapped should be less than π. When the noise level is 1.2π [Fig. 7(d1)], which is a few cases in mining areas, the recoverable deformation gradient of FCNet-CA is about 2 rad/pixel. For interferograms with noise levels greater than 1.2π [Fig. 7(e1) and (f1)], and they are extreme cases, the MUE and STD of FCNet-CA and PUNet begin to diverge uncontrollably and cannot be maintained within a tolerable range. From the overall trend, when the noise becomes more serious, compared with PUNet, FCNet-CA has lower MUE and STD in the simulated interferogram with larger deformation gradient, which indicates that FCNet-CA has stronger antinoise ability.

From the above analysis, it can be seen that the FCNet-CA method has a strong antinoise ability and can break through the theoretical assumptions of the existing unwrapping methods and realize the recovery of surface deformation with a deformation gradient greater than π rad/pixel.

B. Case Study

To further test the performance of the proposed algorithm, FCNet-CA is applied in the Shilawusu coal mine, Inner Mongolia Autonomous Region, China [Fig. 8(a)]. The mining time of the working panel [orange rectangle in Fig. 8(b)] is from September 20, 2016 to May 9, 2017. The mining direction of the working panel is from north to south, and the working panel is 340-m wide and 835-m long. The mining depth is 690 m; the coal seam has a thickness of 5.33 m and an inclination angle of 2°. Most of the surface of the study area is covered by aeolian sand with sparse vegetation. To study the law of surface deformation and ensure the safety of buildings and people on the surface, many leveling monitoring stations are built above the surface of the working panel, i.e., 22 observation stations from A11 to A32 in the strike direction [black points in Fig. 8(c)], with an average distance between two points of 51 m and 22 observation stations from B1 to B22 in the dip direction [red points in Fig. 8(c)], with an average distance between two points of 57 m. In the experiment, two Sentinel-1A images from December 18, 2016 and April 17, 2017, with a single polarization mode (VV), are used. The corresponding SAR image has a resolution of 20 m (range direction) $\times$ 5 m (azimuth direction), a temporal baseline of 120 days, and a perpendicular baseline of approximately 73 m.

To analyze the performance of different unwrapping methods, the unwrapping algorithms that performed well in the simulation experiments are selected as a comparative analysis, i.e., MCF and PUNet methods. Like the simulation experiment, the interferograms are first filtered using Goldstein filtering before unwrapping using MCF and PUNet.

The original interferogram, filtered interferogram, and coherence map of the filtered interferogram are shown in Fig. 9(a)–(c), respectively, and the unwrapping results obtained by MCF, PUNet, and FCNet-CA are shown in Fig. 9(d)–(f), respectively.

It can be seen from Fig. 9 that the interferogram quality in Fig. 9(a) is low as serious temporal decorrelation noise because of the long temporal baseline, and the interferometric fringes are unclear, especially for the center area. Therefore, even the interferogram after Goldstein filtering still has poor phase quality and coherence [Fig. 9(b) and (c)]. Fig. 9(d) shows that the MCF method cannot effectively recover the deformation pattern and magnitude in the center area (red box A). PUNet can barely recover the deformation pattern and magnitude in the center area (red box A), and there are apparent unwrapping errors in the weak deformation region [as shown in white box B in Fig. 9(e)]. Compared to the unwrapped results of MCF and PUNet, the unwrapped results of FCNet-CA [Fig. 9(f)] show that the deformation pattern and magnitude are well restored, and there is no noticeable unwrapped error.

To further quantitatively evaluate the reliability of the unwrapping results, the unwrapped phase is converted into vertical deformation (ignoring the influence of horizontal displacement) and compared with the leveling data [Fig. 10(a) and (b)]. Fig. 10(a) shows that although the results obtained by MCF and PUNet can reflect the deformation trend to a certain extent in the strike direction, both are overestimated in value, especially for PUNet, and have a more significant deviation from the leveling data. In contrast, the results of FCNet-CA are closest to the leveling data. The comparison results in the dip direction are consistent with the strike direction [Fig. 10(b)], and the corresponding RMSE of FCNet-CA is the lowest, followed by MCF and, finally PUNet (Table IV). Compared with PUNet and MCF, Table IV shows the RMSE of FCNet-CA in the strike direction is reduced by 67.9% and 29.5%, respectively, and the RMSE of FCNet-CA in the dip direction is reduced by 72.4% and 50.9%, respectively.

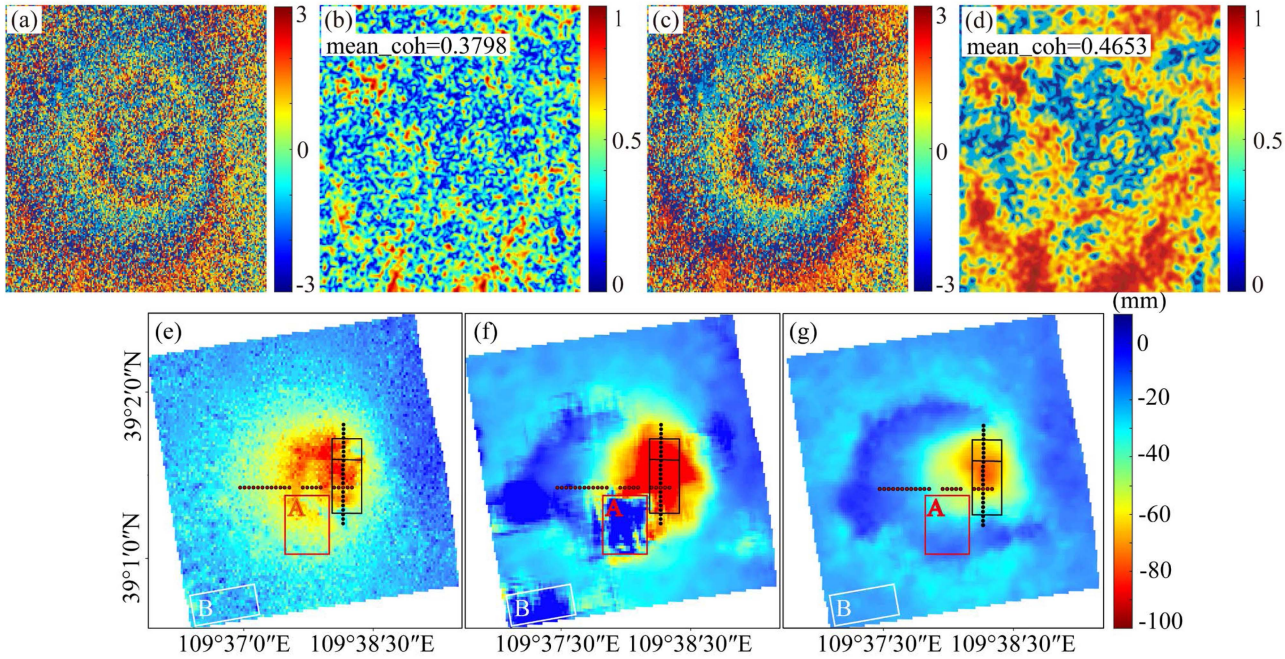

Fig. 9. Interferogram of the study area and three unwrapping algorithms' results, including (a) original interferogram, (b) original coherence map, (c) interferogram after Goldstein filtering [44], (d) coherence map after Goldstein filtering, (e) deformation recovered by MCF, (f) deformation recovered by PUNet, and (g) deformation recovered by FCNet-CA.

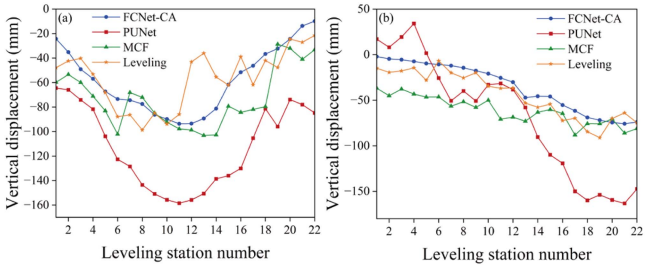

Fig. 10. Comparison results of three algorithms. (a) Comparison results of FCNet-CA, PUNet, MCF, and leveling data in the strike direction. (b) Comparison results of FCNet-CA, PUNet, MCF, and leveling data in the dip direction.

TABLE IV
RMSES AND RUNTIME COMPARISONS OF DIFFERENT UNWRAPPING METHODS

Methods	Strike direction RMSE (mm)	Dip direction RMSE (mm)	Runtime (s)
MCF	28.1	23.2	0.12
PUNet	61.7	41.3	0.33
FCNet-CA	**19.8**	**11.4**	**0.17**

It should be noted that the experimental results here are not consistent with those of the simulation experiment. PUNet performs better than MCF in the simulation experiment, but MCF performs better than PUNet for the actual data. This phenomenon may be explained by the fact that although the atmospheric disturbance, the complex Gaussian noise, and decorrelation noise caused by water are considered in the processing of sample generation in the simulation experiment, the temporal decorrelation noise, which seriously affects the quality of the interferogram in this case, is not fully considered. This is consistent with the characteristics of PUNet, which lack consideration of temporal decorrelation factors and results in poor unwrapping performance of interferograms with long temporal baselines.

IV. DISCUSSION

The training dataset is very significant in the performance and generalizability of DCNN. Generally, the more diverse the samples in the training dataset, the more features the network can learn, resulting in better generalization performance. Different sample generation strategies are employed to investigate the impact of various training sample sets on network performance, i.e., 2-D Gaussian surface method, mining subsidence model, and new strategy proposed in Section II-A to train FCNet-CA, respectively. The setting of parameters for each method is consistent with Section II-A. Every method generates training datasets containing 30 000 simulated interferograms, and the trained networks are applied to the interferometric phase unwrapping of the Shilawusu coal mine. The unwrapping results under different training samples strategies are shown in Fig. 11(a)–(d), respectively. Fig. 11(a) and (b) shows that the deformation center area recovered by different networks trained with the same training dataset is roughly the same, but FCNet-CA [Fig. 11(b)] recovers the deformation pattern better than PUNet [Fig. 11(a)] under the same training strategy. There are no apparent unwrapping errors in the weak deformation region C. Fig. 11(c) shows that phase information recovery of the network trained with mixed samples is more complete and smoother. In contrast, the unwrapping results of the network obtained by only using the

TABLE V
RESULTS OF NETWORK UNWRAPPING ERRORS TRAINED WITH DIFFERENT TRAINING SETS

Methods \ Datasets	Two-dimensional Gaussian surface	Proposed method	Mining subsidence model	Strike direction RMSE (mm)	Dip direction RMSE (mm)
PUNet	√			61.7	41.3
FCNet-CA	√			28.8	13.9
FCNet-CA		√		**19.8**	**11.4**
FCNet-CA			√	27.4	15.4

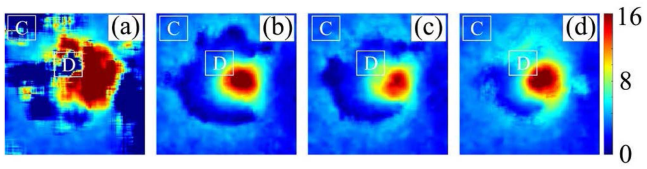

Fig. 11. Unwrapping results under different training samples. (a) PUNet unwrapping results trained with two-dimensional Gaussian surface samples. (b) FCNet-CA unwrapping results trained with two-dimensional Gaussian surface samples. (c) FCNet-CA unwrapping results trained with the proposed method. (d) FCNet-CA unwrapping results with samples generated with mining subsidence model.

samples generated by the mining subsidence model have some errors in the deformation center area [white box D in Fig. 11(d)], which indicates that the samples generated by a single mining subsidence model cannot thoroughly learn the characteristics of the surface subsidence basin. Comparing Fig. 11(b) with (d), it can be found that for FCNet-CA, the main deformation centers can be effectively recovered under different training samples, but the deformation center's absolute phase is somewhat overestimated under a single training sample. Compared with that in Fig. 11(c) and (d), FCNet-CA with the proposed training method [Fig. 11(c)] has a better effect on recovering the deformation pattern and magnitude, and there is no noticeable error.

Table V shows that under the same training strategy (2-D Gaussian surface method), compared with those of PUNet, the RMSEs of FCNet-CA in the strike and dip directions decreased by 53.3% and 66.3%, respectively. The RMSEs of FCNet-CA under different single training dataset (2-D Gaussian surface method and mining subsidence prediction model) is similar. Compared with the 2-D Gaussian surface method and mining subsidence prediction model, the RMSEs of FCNet-CA under the proposed training strategy in the strike direction are reduced by 31.3% and 27.7%, respectively, and the RMSEs in the dip direction are reduced by 18% and 26%, respectively.

Experimental results further prove that FCNet-CA is more robust and has higher unwrapping accuracy under low coherence conditions. Moreover, the training strategy proposed in this article can effectively improve network performance and generalization ability.

It is worth mentioning that the part of phase feature extraction and phase information reconstruction in the FCNet-CA is similar to the PUNet. However, we add the SE block to the end of phase feature extraction to help FCNet-CA better extract the feature

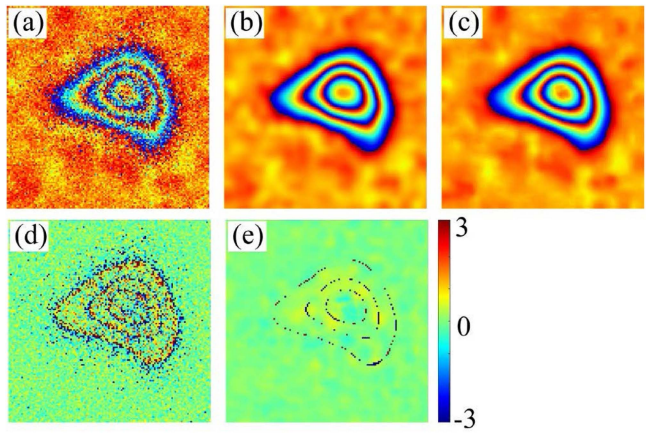

Fig. 12. Comparison between the original phase and rewrapped phase. (a) Original interferogram with noise. (b) Rewrapped result of the absolute clean phase. (c) Rewrapped result of the unwrapped phase obtained by FCNet-CA. (d) Difference between (a) and (c). (e) Difference between (b) and (c).

from the noise, even if the noise is severe. In the part of phase information reconstruction, we replace the simple convolution layer with the bottleneck, which is beneficial to train a deeper network while reducing the parameters of the network. In addition, FCNet-CA needs more time to train due to the property of the fully convolutional structure. Although we try to use transfer learning to reduce the training cost, it is still difficult to train the FCNet-CA. It is of future interest to design a lightweight network to reduce the training cost.

The incongruent problem usually exists in the one-step method. The incongruent problem means that the rewrapped result of the unwrapped phase obtained by the one-step method is different from the original interferogram. The simulated interferogram from sample 2 of Fig. 6(a) is used to show the incongruent problem, as seen in Fig. 12.

The rewrapped phase of the FCNet-CA [Fig. 12(c)] has a consistent number of fringes with the rewrapped result of the absolute phase [Fig. 12(b)] and only has some error in the place of phase jump [Fig. 12(e)]. The rewrapped errors [Fig. 12(d)] contain random noise and errors in the place of phase jump, which are the main drawback of the FCNet-CA. Trying to use the two-step deep-learning-based method to avoid the incongruent problem by changing the structure and output of the FCNet-CA is the direction of the subsequent work.

V. Conclusion

Existing unwrapping methods often fail to unwrap the interferogram of mining areas with considerable noise and dense fringes. In comparison to the current unwrapping methods, FCNet-CA has the following advantages: 1) phase unwrapping can be performed without phase filtering; 2) the interferometric phase can be recovered under different noise levels and deformation gradient scenarios; 3) the unwrapping accuracy is greatly improved, and 4) based on the mining subsidence model, a new sample generation strategy is proposed that generates training samples that are closer to the actual geological mining conditions, thus improving the generalizability performance of the network.

In this article, FCNet-CA is compared with the existing methods through simulation experiments and actual cases. The simulation experiment results are as follows: 1) the average STD of FCNet-CA is 0.4, which is 68.8%, 87.3%, 89.7%, 86.6%, 80.5%, and 90.6% and 93.8% lower than that of PUNet, DLPU, MCF, LS, PUMA, BC, and QGPU, respectively; 2) the proportion of $|\varepsilon| \leq 1$ in FCNet-CA can reach 91.3%, which is significantly higher than that of 53% in PUNet, 28.3% in MCF, 24.3% in DLPU, 13.3% in LS, 7.8% in PUMA, 6.3% in BC, and 1.9% in QGPU; and 3) traditional unwrapping methods, such as MCF, can work well in areas with good coherence and gradients less than π, or fewer arcs with gradients exceeding π. Compared with traditional methods, FCNet-CA can better recover the deformation pattern and magnitude with higher accuracy under high noise and high fringe density (even if the phase gradient exceeds π). The experimental results of actual cases show that compared with the RMSEs of PUNet and MCF, the RMSE of FCNet-CA in the strike direction is reduced by 67.9% and 29.5%, respectively, and the RMSE of FCNet-CA in the dip direction is reduced by 72.4% and 50.9%, respectively.

The SAR sensor type and polarization mode can have a certain impact on the sample dataset and deep-learning network construction, and the learning samples generated by geological mining conditions in different mining areas are also different. This article does not consider the influence of different SAR image sensors and different polarization modes on deep-learning network construction and sample training and only generates learning samples under some geological mining conditions. In future article, a unified framework of deep-learning networks will be established for different types of SAR sensors with different polarization modes. At the same time, according to different geological mining conditions, the training samples will be further enriched, and the network's generalization ability will be improved to provide a guarantee for the better application of InSAR technology in monitoring surface deformation in mining regions.

References

[1] F. Bell, T. Stacey, and D. Genske, "Mining subsidence and its effect on the environment: Some differing examples," *Environ. Geol.*, vol. 40, pp. 135–152, 2000.

[2] B. Chen et al., "Three-dimensional time-varying large surface displacements in coal exploiting areas revealed through integration of SAR pixel offset measurements and mining subsidence model," *Remote Sens. Environ.*, vol. 240, 2020, Art. no. 111663.

[3] B. Chen, K. Deng, H. Fan, and Y. Yu, "Combining SAR interferometric phase and intensity information for monitoring of large gradient deformation in coal mining area," *Eur. J. Remote Sens.*, vol. 48, no. 1, pp. 701–717, 2015.

[4] B. Chen, H. Mei, Z. Li, Z. Wang, Y. Yu, and H. Yu, "Retrieving three dimensional large surface displacements in coal mining areas by combining SAR pixel offset measurements with an improved mining subsidence model," *Remote Sens.*, vol. 13, no. 13, 2021, Art. no. 2541.

[5] B. Chen et al., "Time-varying surface deformation retrieval and prediction in closed mines through integration of SBAS InSAR measurements and LSTM algorithm," *Remote Sens.*, vol. 14, no. 3, 2022, Art. no. 788.

[6] R. M. Goldstein, H. A. Zebker, and C. L. Werner, "Satellite radar interferometry: Two-dimensional phase unwrapping," *Radio Sci.*, vol. 23, no. 4, pp. 713–720, 1988.

[7] W. Xu and I. Cumming, "A region-growing algorithm for InSAR phase unwrapping," *IEEE Trans. Geosci. Remote Sens.*, vol. 37, no. 1, pp. 124–134, Jan. 1999.

[8] M. Costantini, "A novel phase unwrapping method based on network programming," *IEEE Trans. Geosci. Remote Sens.*, vol. 36, no. 3, pp. 813–821, May 1998.

[9] K. Itoh, "Analysis of the phase unwrapping algorithm," *Appl. Opt.*, vol. 21, no. 14, pp. 2470–2470, 1982.

[10] Y. LeCun, Y. Bengio, and G. Hinton, "Deep learning," *Nature*, vol. 521, no. 7553, pp. 436–444, 2015.

[11] H. Yu, T. Yang, L. Zhou, and Y. Wang, "PDNet: A lightweight deep convolutional neural network for InSAR phase denoising," *IEEE Trans. Geosci. Remote Sens.*, vol. 60, 2022, Art. no. 5239309.

[12] S. Vitale, G. Ferraioli, V. Pascazio, and G. Schirinzi, "InSAR-MONet: Interferometric SAR phase denoising using a multiobjective neural network," *IEEE Trans. Geosci. Remote Sens.*, vol. 60, 2022, Art. no. 5239814.

[13] W. Yang et al., "A deep convolutional neural network with multiscale feature dynamic fusion for InSAR phase filtering," *IEEE J. Sel. Topics Appl. Earth Observ. Remote Sens.*, vol. 15, pp. 6687–6710, 2022.

[14] B. Ghosh, M. Motagh, M. H. Haghighi, M. S. Vassileva, T. R. Walter, and S. Maghsudi, "Automatic detection of volcanic unrest using blind source separation with a minimum spanning tree based stability analysis," *IEEE J. Sel. Topics Appl. Earth Observ. Remote Sens.*, vol. 14, pp. 7771–7787, 2021.

[15] N. I. Bountos, D. Michail, and I. Papoutsis, "Learning from synthetic InSAR with vision transformers: The case of volcanic unrest detection," *IEEE Trans. Geosci. Remote Sens.*, vol. 60, 2022, Art. no. 4509712.

[16] H. Zhou, K. Dai, S. Pirasteh, R. Li, J. Xiang, and Z. Li, "InSAR spatial-heterogeneity tropospheric delay correction in steep mountainous areas based on deep learning for landslides monitoring," *IEEE Trans. Geosci. Remote Sens.*, vol. 61, 2023, Art. no. 5215014.

[17] J. Hu, W. Wu, R. Gui, Z. Li, and J. Zhu, "Deep learning-based homogeneous pixel selection for multitemporal SAR interferometry," *IEEE Trans. Geosci. Remote Sens.*, vol. 60, 2022, Art. no. 5234518.

[18] T. Yang, H. Yu, and Y. Wang, "Selection of persistent scatterers with a deep convolutional neural network," in *Proc. IEEE Int. Geosci. Remote Sens. Symp.*, 2022, pp. 2912–2915.

[19] D. Carcereri, P. Rizzoli, D. Ienco, and L. Bruzzone, "A deep learning framework for the estimation of forest height from bistatic TanDEM-X data," *IEEE J. Sel. Topics Appl. Earth Observ. Remote Sens.*, vol. 16, pp. 8334–8352, 2023.

[20] F. L. Zhou, H. Yu, Y. Lan, and M. Xing, "Deep learning-based branch-cut method for InSAR two-dimensional phase unwrapping," *IEEE Trans. Geosci. Remote Sens.*, vol. 60, 2022, Art. no. 5209615.

[21] K. Yang, Z. Yuan, X. Xing, and L. Chen, "Deep-learning-based mask-cut method for InSAR phase unwrapping," *IEEE J. Miniaturization Air Space Syst.*, vol. 4, no. 2, pp. 221–230, Jun. 2023.

[22] H. Yu, Y. Zhou, S. S. Ivey, and Y. Lan, "Large-scale multibaseline phase unwrapping: Interferogram segmentation based on multibaseline envelope-sparsity theorem," *IEEE Trans. Geosci. Remote Sens.*, vol. 57, no. 11, pp. 9308–9322, Nov. 2019.

[23] Z. Yuan, Z. Lu, L. Chen, and X. Xing, "A closed-form robust cluster-analysis-based multibaseline InSAR phase unwrapping and filtering algorithm with optimal baseline combination analysis," *IEEE Trans. Geosci. Remote Sens.*, vol. 58, no. 6, pp. 4251–4262, Jun. 2020.

[24] Z. Yuan, T. Chen, H. Yu, W. Peng, L. Chen, and X. Xing, "Cluster correction for cluster analysis-based multibaseline InSAR phase unwrapping," *IEEE J. Sel. Topics Appl. Earth Observ. Remote Sens.*, vol. 15, pp. 8600–8612, 2022.

[25] L. Zhou, H. Yu, Y. Lan, and M. Xing, "Artificial intelligence in interferometric synthetic aperture radar phase unwrapping: A review," *IEEE Geosci. Remote Sens. Mag.*, vol. 9, no. 2, pp. 10–28, Jun. 2021.
[26] K. Wang, Y. Li, Q. Kemao, J. Di, and J. Zhao, "One-step robust deep learning phase unwrapping," *Opt. Exp.*, vol. 27, no. 10, pp. 15100–15115, 2019.
[27] Z. Wu, T. Wang, Y. Wang, R. Wang, and D. Ge, "Deep learning for the detection and phase unwrapping of mining-induced deformation in large-scale interferograms," *IEEE Trans. Geosci. Remote Sens.*, vol. 60, 2022, Art. no. 5216318.
[28] L. Zhou, H. Yu, V. Pascazio, and M. Xing, "PU-GAN: A one-step 2-D InSAR phase unwrapping based on conditional generative adversarial network," *IEEE Trans. Geosci. Remote Sens.*, vol. 60, 2022, Art. no. 5221510.
[29] G. Spoorthi, S. Gorthi, and R. K. S. S. Gorthi, "Phasenet: A deep convolutional neural network for two-dimensional phase unwrapping," *IEEE Signal Process. Lett.*, vol. 26, no. 1, pp. 54–58, Jan. 2019.
[30] G. Spoorthi, R. K. S. S. Gorthi, and S. Gorthi, "Phasenet 2.0: Phase unwrapping of noisy data based on deep learning approach," *IEEE Trans. Image Process.*, vol. 29, pp. 4862–4872, 2020.
[31] L. Zhou, H. Yu, and Y. Lan, "Deep convolutional neural network-based robust phase gradient estimation for two-dimensional phase unwrapping using SAR interferograms," *IEEE Trans. Geosci. Remote Sens.*, vol. 58, no. 7, pp. 4653–4665, Jul. 2020.
[32] J. Litwiniszyn, "Stochastic methods in mechanics of granular bodies," in *Stochastic Methods in Mechanics of Granular Bodies: CourseHeld at the Department of General Mechanics*. Berlin, Germany: Springer-Verlag, 1974, pp. 5–9.
[33] E. Maggiori, Y. Tarabalka, G. Charpiat, and P. Alliez, "Convolutional neural networks for large-scale remote-sensing image classification," *IEEE Trans. Geosci. Remote Sens.*, vol. 55, no. 2, pp. 645–657, Feb. 2017.
[34] S. Ioffe and C. Szegedy, "Batch normalization: Accelerating deep network training by reducing internal covariate shift," in *Proc. Int. Conf. Mach. Learn.*, 2015, pp. 448–456.
[35] C. Guo, B. Fan, Q. Zhang, S. Xiang, and C. Pan, "AugFPN: Improving multi-scale feature learning for object detection," in *Proc. IEEE/CVF Conf. Comput. Vis. Pattern Recognit.*, 2020, pp. 12592–12601.
[36] J. Hu, L. Shen, and G. Sun, "Squeeze-and-excitation networks," in *Proc. IEEE Conf. Comput. Vis. Pattern Recognit.*, 2018, pp. 7132–7141.
[37] N. Tishby and N. Zaslavsky, "Deep learning and the information bottleneck principle," in *Proc. IEEE Inf. Theory Workshop*, 2015, pp. 1–5.
[38] K. He, X. Zhang, S. Ren, and J. Sun, "Deep residual learning for image recognition," in *Proc. IEEE Conf. Comput. Vis. Pattern Recognit.*, 2016, pp. 770–778.
[39] K. Simonyan and A. Zisserman, "Very deep convolutional networks for large-scale image recognition," in *Proc. Int. Conf. Learn. Representat.*, 2015, pp. 1–14.
[40] S. J. Pan and Q. Yang, "A survey on transfer learning," *IEEE Trans. Knowl. Data Eng.*, vol. 22, no. 10, pp. 1345–1359, Oct. 2010.
[41] P. J. Huber, "Robust estimation of a location parameter," in *Breakthroughs in Statistics: Methodology and Distribution*. Berlin, Germany: Springer-Verlag, 1992, pp. 492–518.
[42] J. M. Bioucas-Dias and G. Valadao, "Phase unwrapping via graph cuts," *IEEE Trans. Image Process.*, vol. 16, no. 3, pp. 698–709, Mar. 2007.
[43] D. C. Ghiglia and L. A. Romero, "Minimum Lp-norm two-dimensional phase unwrapping," *J. Oper. Strategic Anal. A*, vol. 13, no. 10, pp. 1999–2013, 1996.
[44] R. M. Goldstein and C. L. Werner, "Radar interferogram filtering for geophysical applications," *Geophys. Res. Lett.*, vol. 25, no. 21, pp. 4035–4038, 1998.

Yu Yang received the B.Eng. degree in surveying engineering from the Jiangsu Normal University, Jiangsu, China, in 2021. He is currently working toward the M.Eng. degree in electronic and information engineering with the Jiangsu Normal University.

His research interests include InSAR data processing and application.

Bingqian Chen received the Ph.D. degree in geodesy from the China University of Mining and Technology, Xuzhou, China, in 2015.

He is currently an Associate Professor with the School of Geography, Geomatics and Planning, Jiangsu Normal University, Jiangsu, China. His research interests include radar data processing, mining subsidence monitoring and prediction, optimization algorithms, data fusion, and high-performance machine-learning approaches for large-scale data analysis.

Zhenhong Li (Senior Member, IEEE) received the B.Eng. degree in geodesy from the Wuhan Technical University of Surveying and Mappingg (now Wuhan University), Wuhan, China, in 1997, and the Ph.D. degree in GPS, geodesy, and navigation from the University College London, London, U.K., in 2005.

He is currently a Professor of imaging geodesy with the College of Geological Engineering and Geomatics, Chang'an University, Xi'an, China, and a Visiting Professor with the School of Engineering, Newcastle University, Newcastle upon Tyne, U.K. He is also the Principal Investigator of the Generic Atmospheric Correction Online Service for interferometric synthetic aperture radar. His research interests include space geodesy and remote sensing (mainly InSAR and GNSS) and their applications to geohazards (e.g., earthquakes, landslides, and land subsidence) and precision agriculture.

Prof. Li is a fellow of the International Association of Geodesy and an Associate Editor for Advances in Space Research and Remote Sensing.

Chen Yu received the bachelor's degree in geographic information system (GIS) from Sun Yat-sen University and the master's degree in geodesy and surveying engineering from Wuhan University. He recieved the Ph.D. degree in geodesy from Newcastle University, U.K. He is currently a Professor with the College of Geological Engineering and Geomatics, Chang'an University, Xi'an, China. His research interests include monitoring and interpreting geohazards such as earthquakes, volcanoes, landslides, and ground subsidence using a variety of Earth Observations. His main objective is to develop a geohazard early warning system with the capacity of early-stage hazard detection and pre-warning, risk assessment of the hazard affected area, and rapid responding to catastrophic events.

Chuang Song was born in Heze, China, in 1994. He received the B.S. degree in geomatics from the Southwest Jiaotong University, Chengdu, China, in 2015, the M.Sc. degree in geodesy from the Wuhan University, Wuhan, China, in 2018, and the Ph.D. degree in geodesy from the Newcastle University, Newcastle upon Tyne, U.K., in 2022.

He is currently a Lecturer with the College of Geological Engineering and Geomatics, Chang'an University, Xi'an, China. His research interest includes the processing of satellite radar data and its application in the study of natural hazards (such as landslides and earthquakes).

Fengcheng Guo was born in 1992. He received the Ph.D. degree in photogrammetry and remote sensing from the State Key Laboratory of Information Engineering in Surveying Mapping, and Remote Sensing, Wuhan University, Wuhan, China, in 2020.

Since 2020, he has been with the School of Geography, Geomatics and Planning, Jiangsu Normal University, Jiangsu, China, where he became an Associate Professor in 2022. His research interest includes SAR image processing.